General Approach for Modeling and Control of Multiphase PMSM Drives

Andrea Cervone, *Student Member, IEEE*, Obrad Dordevic, *Member, IEEE*, and Gianluca Brando

***Abstract*—This article presents a modeling approach and a control strategy for multiphase surface-mounted permanent magnet synchronous machine drives. The mathematical model is completely general with respect to the machine parameters and to the winding configuration. It also intrinsically considers the effects of eventual constraints for the phase currents, generated from the electrical connections among the phase windings or resulting from faults. The current controller is entirely formalized in the phase variables domain. It is based on a pseudoinverse decoupling algorithm and on a linear decoupled controller. The current references are computed by means of a maximum-torque-per-ampere strategy, which can be also easily adapted for torque sharing purposes. The proposed controller requires minimum changes with respect to system reconfigurations or parameters variations and, therefore, it is suited both for healthy and for faulty operations. An extensive set of experimental results has been conducted to validate the proposed approach in several testing scenarios.**

***Index Terms*—Decoupled control, multiphase drives, multiphase machines, permanent magnet synchronous machines, phase variables control.**

NOMENCLATURE

Machine model

n	Number of machine phases
$\boldsymbol{i}_m, \boldsymbol{v}_m$	Machine phase currents, voltages.
$\boldsymbol{\lambda}_m, \boldsymbol{\lambda}_{\mathrm{PM}}$	Machine induced fluxes, PM induced fluxes.
$\boldsymbol{e}_{\mathrm{PM}}, \boldsymbol{f}_{\mathrm{PM}}$	PM induced back-EMFs, normalized back-EMFs.
$\boldsymbol{L},\ \boldsymbol{R}$	Machine inductances matrix, resistances matrix.
$\theta,\ \omega$	Rotor position, angular speed.
P_p	Pole pairs number.
T_{em}	Electromagnetic torque.

Interconnection network model

n_{VSI}	Number of converter legs.
$\boldsymbol{v}_{\mathrm{VSI}}$	Converter controllable voltages set.
$\boldsymbol{N}$	Machine/converter interconnection matrix.
$\boldsymbol{v}_{\mathrm{NET}}$	Network constraints auxiliary voltages set.
$\boldsymbol{M}$	Constraints matrix.
$\boldsymbol{U}_f$	Configuration matrix.

Currents control algorithm

$\boldsymbol{\delta i}_m^*$	Desired currents derivatives set.
$\tilde{\boldsymbol{i}}_m$	Current tracking error set.
$\boldsymbol{v}_{\mathrm{VSI,opt}}^*$	Converter voltages minimum-norm vector.
$\boldsymbol{v}_{\mathrm{VSI,off}}^*$	Converter voltages offset vector.
$\mathcal{L}(\star),\ s$	Laplace transform, Laplace complex variable.
$\mathcal{C}, \mathcal{G}$	Controller, system transfer function.

Reference currents computation strategy

I_{RMS}	Root mean square (rms) current.
$\boldsymbol{W}$	MTPA weighting matrix.
$\mathfrak{L},\ \mu,\ \boldsymbol{\nu}$	Lagrangian function, Lagrange multipliers.

Matrix formalism

$\star^{\mathrm{T}}, \star^{-1}, \star^{\dagger}$	Transpose, inverse, Moore–Penrose pseudoinverse.

Manuscript received July 1, 2020; revised October 14, 2020 and December 29, 2020; accepted February 25, 2021. Date of publication March 4, 2021; date of current version June 1, 2021. Recommended for publication by Associate Editor A. M. Trzynadlowski. *(Corresponding author: Andrea Cervone.)*

Andrea Cervone and Gianluca Brando are with the Department of Electrical Engineering and Information Technology, University of Naples Federico II, 80125 Naples, Italy (e-mail: andrea.cervone@unina.it; gianluca.brando@unina.it).

Obrad Dordevic is with the Faculty of Engineering and Technology, Liverpool John Moores University, Liverpool L3 3AF, U.K. (e-mail: o.dordevic@ljmu.ac.uk).

Digital Object Identifier 10.1109/TPEL.2021.3063791

I. INTRODUCTION

MULTIPHASE electrical drives are nowadays considered as one of the most promising technologies from the electrical scientific community [1]–[4]. A multiphase drive offers several advantages when compared to its three-phase counterpart as follows.

1) The input power can be split into more phases, thus reducing the voltage and/or current requirements for the semiconductor devices of the converter.
2) The machine can continue operating even in case of faults of one or more phases, although with reduced capabilities.
3) More spatial harmonics of the magnetic flux density at the air-gap can be exploited to develop the desired electromagnetic torque by using nonsinusoidal currents.
4) The overall torque and/or power can be unevenly shared among different winding subsets.

This article focuses on drives based on multiphase surface mounted permanent magnet synchronous machines (PMSMs).

Standard modeling approaches for multiphase machines are based on the vector space decomposition (VSD). The machine phase currents are linearly combined, through a generalized Clarke's transformation matrix, into a set of space vectors, each of which drives a set of spatial harmonics of the magnetic flux density at the air-gap [1], [2]. The developed electromagnetic torque is given by the interaction of each stator-generated harmonic with the corresponding harmonic produced by the rotor permanent magnets (PMs). Given the finite number of phases, not all the harmonics can be simultaneously controlled.

Therefore, the choice of a proper set of controllable space vectors is crucial. Also note that the VSD transformation matrix formalization is not a trivial process, since it depends both on the winding configuration (e.g., symmetrical or asymmetrical) and on their connection (e.g., open-end terminals, single/multiple isolated neutral points, etc.) [5]. In this context, the most used control techniques for multiphase drives are derived from the three-phase ones [1]–[3], especially from the direct torque control (DTC) and the field oriented control (FOC). DTC algorithms typically rely on optimal switching tables and are based on the simultaneous control of the electromagnetic torque and the fundamental component of the stator flux. FOC algorithms are based on a rotational transformation applied to the VSD model, which projects each variable in a rotating reference frame synchronous with the corresponding spatial harmonic component. The torque control is then obtained by driving the synchronous currents towards constant references and is usually realized with proportional-integral (PI) controllers.

In case of symmetrical machines, the VSD approach always guarantees the decoupling of each current space vector dynamics from the others. On the contrary, in case of structural disbalances (e.g., postfault operations, asymmetrical magnetic axes disposition, unequal number of turns, etc.) this property might not be guaranteed, leading to undesired coupling effects among different space vector components, which should be properly neutralized. Moreover, the torque control may require unequal current waveforms in different phases and may even require the exploitation of additional current harmonics.

Different approaches have been proposed to overcome these issues. In [6], it has been shown that with asymmetrical magnetic axes disposition it might be impossible to control certain space vector sets at the same time. Moreover, additional coupling terms exist among the current components in the multiple synchronous domain, which have been neutralized through proper compensations.

Another commonly used modeling approach is the multistator one, where the machine phases are grouped in symmetrical sets, which are controlled independently from one another. However, the same coupling problem is also present and it may even cause instability [7], [8]. For this reason, a proper decoupling algorithm should be implemented [9]–[11].

Similar effects can be seen in many postfault operations: for example, an n-phase machine subjected to an open-circuit fault can be considered as an asymmetrical $(n-1)$-phase machine. In some works, the open-circuit faults have been formalized through additional algebraic constraints among the VSD transformed currents [12]–[14]. Thanks to an ad hoc machine design, Locment *et al.* [12] and Baudart *et al.* [13] realized the current controller similarly to healthy conditions, while Yu *et al.* [14] recurred to hysteresis controllers with high control and switching frequency. Other approaches [15]–[20] modeled the fault directly in the phase-variables domain, but have been mainly focused on the references computation strategy. The dynamic coupling effects have not been investigated, and again they were neutralized through high bandwidth hysteresis controllers [16]–[20].

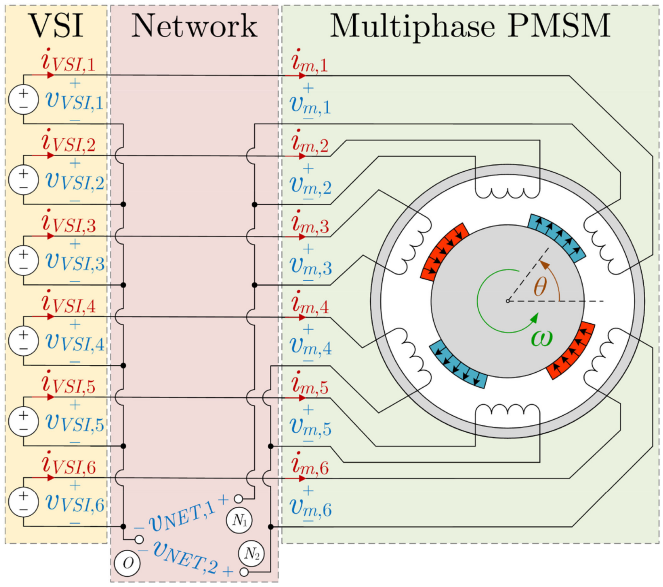

Fig. 1. System architecture for a six-phase PMSM ($n = 6$) supplied by a six-phase VSI ($n_{\mathrm{VSI}} = 6$) and with two isolated neutral points ($n_c = 2$).

This article presents a modeling approach and a control algorithm for multiphase surface-mounted PMSM drives by which the abovementioned problems will be automatically covered. The main contribution of this article in this field is the flexibility and generality of this novel approach, which is easily adaptable to different machine parameters, configurations, and control requirements.

This article is structured as follows. The mathematical model of the machine, derived in the phase variables domain, is discussed in Section II. Section III focuses on the currents control algorithm which, contrarily to most of the standard approaches, is also completely derived in the phase variables domain and does not involve any VSD or rotational transformation. The computation of the current references using a maximum-torque-per-ampere (MTPA) approach is discussed in Section IV. The overall control scheme is summarized in Section V. The experimental validation of the proposed approach, using a nine-phase PMSM setup in several testing scenarios, is provided in Sections VI and VII. Finally, Section VIII concludes this article.

II. Mathematical Model

The machine under analysis is an n-phase surface-mounted PMSM, supplied by an n_{VSI}-leg voltage source inverter (VSI) through an interconnection network of a known structure (see Fig. 1). In this section, the mathematical models of the machine and of the whole drive are derived.

A. Machine Model

Under the linearity hypothesis, the flux induced in each of the n stator windings is given by the superimposed contribution of the magnetic field density produced by all the phase currents and by the permanent magnets on the rotor. By using matrix

notation, this relationship can be expressed as

$$\boldsymbol{\lambda}_m = \boldsymbol{L} \cdot \boldsymbol{i}_m + \boldsymbol{\lambda}_{\mathrm{PM}}(\theta) \tag{1}$$

where $\boldsymbol{\lambda}_m$ is the $n \times 1$ vector of winding fluxes, $\boldsymbol{i}_m$ is the $n \times 1$ vector of phase currents, $\boldsymbol{L}$ is the $n \times n$ inductances matrix, and $\boldsymbol{\lambda}_{\mathrm{PM}}$ is the $n \times 1$ vector of PM induced flux linkages.

Each kth PM induced flux $\lambda_{\mathrm{PM},k}$ is a periodic function of the rotor position θ. Then, a Fourier decomposition in the interval $\theta \in [0; 2\pi]$ allows identifying the contribution of each spatial harmonic. Note that the pole-pair periodicity is implicitly defined through the flux vector function $\boldsymbol{\lambda}_{\mathrm{PM}}(\theta)$. As an example, for an ideal sinusoidal machine with P_p pole pairs, each PM induced flux is a pure sinusoidal function of $P_p \cdot \theta$, meaning that only the harmonic of order P_p is present.

For a surface-mounted PMSM, the inductances matrix $\boldsymbol{L}$ does not depend on the rotor position θ and is always guaranteed to be symmetric and positive definite (for energy-related reasons).

Each winding terminal voltage is given by the contribution of the resistive drop and the induced back-EMFs

$$\boldsymbol{v}_m = \boldsymbol{R} \cdot \boldsymbol{i}_m + \boldsymbol{L} \cdot \frac{\mathrm{d}\boldsymbol{i}_m}{\mathrm{d}t} + \boldsymbol{e}_{\mathrm{PM}} \tag{2}$$

where $\boldsymbol{v}_m$ is the $n \times 1$ vector of winding terminal voltages, $\boldsymbol{e}_{\mathrm{PM}}$ is the $n \times 1$ vector of PM induced back-EMFs, and $\boldsymbol{R}$ is the $n \times n$ resistances matrix.

Since the resistive voltage drop of each phase only depends on the corresponding current, $\boldsymbol{R}$ is a diagonal matrix whose elements are the winding resistances. As a result, $\boldsymbol{R}$ is positive definite. Naturally, in case all the machine windings have the same resistance, $\boldsymbol{R}$ is a scalar matrix (i.e., $\boldsymbol{R} = R \cdot \boldsymbol{I}$).

The PM induced back-EMFs can be expressed as

$$\boldsymbol{e}_{\mathrm{PM}} = \frac{\mathrm{d}\boldsymbol{\lambda}_{\mathrm{PM}}}{\mathrm{d}t} = \frac{\partial \boldsymbol{\lambda}_{\mathrm{PM}}}{\partial \theta} \cdot \frac{\mathrm{d}\theta}{\mathrm{d}t} = \boldsymbol{f}_{\mathrm{PM}}(\theta) \cdot \omega \tag{3}$$

where $\omega = \mathrm{d}\theta/\mathrm{d}t$ is the angular speed of the rotor, while $\boldsymbol{f}_{\mathrm{PM}}(\theta) = \partial \boldsymbol{\lambda}_{\mathrm{PM}}/\partial \theta$ is the set of normalized PM induced back-EMFs, which are also periodic functions of θ.

For the energy conservation principle, the electromagnetic torque developed by the machine is expressed as

$$T_{em} = \sum_{k=1}^{n} \frac{\partial \lambda_{\mathrm{PM},k}}{\partial \theta} \cdot i_{m,k} = \sum_{k=1}^{n} f_{\mathrm{PM},k} \cdot i_{m,k} = \boldsymbol{f}_{\mathrm{PM}}^{\mathrm{T}} \cdot \boldsymbol{i}_m. \tag{4}$$

Therefore, the torque is a linear combination of the machine phase currents, weighted (for each rotor position) by the corresponding normalized PM induced back-EMFs.

B. Electrical Connection Model

The machine windings are connected to each other and to the supply converter through a known interconnection network, here modeled as a linear time-invariant system. Those physical connections (number of neutral connections, or unconnected phases) define certain constraints for the machine currents by Kirchhoff's current law. A simple example of such constraints is represented by an isolated neutral point, which forces the sum of the currents of the corresponding windings to zero. Since the phase currents are state variables for the system, these constraints should be properly considered in the machine model. The n_c algebraic constraints, where $n_c \leq n$, can be imposed by nullifying some linear combinations of the phase currents. Consequently, by adopting a matrix approach, they can be formalized as

$$\boldsymbol{M}^{\mathrm{T}} \cdot \boldsymbol{i}_m = \boldsymbol{0} \tag{5}$$

where $\boldsymbol{M}$ is a $n \times n_c$ full-ranked matrix. For example, considering the six-phase topology with two isolated neutral points depicted in Fig. 1, it results that $i_{m,1} + i_{m,2} + i_{m,3} = 0$ and $i_{m,4} + i_{m,5} + i_{m,6} = 0$, and the corresponding constraints matrix is $\boldsymbol{M} = [1\,1\,1\,0\,0\,0;\ 0\,0\,0\,1\,1\,1]^{\mathrm{T}}$ (where semicolon sign is used to separate the two matrix rows).

The effect of the algebraic constraints on the electrical equations of the machine can be modeled by introducing an additional $n_c \times 1$ set of voltages $\boldsymbol{v}_{\mathrm{NET}}$.

For a pulsewidth-modulated converter each kth phase leg (with $k = 1, \ldots, n_{\mathrm{VSI}}$) can be modeled with a controllable voltage source $v_{\mathrm{VSI},k}$ identifying the average voltage supplied in a modulation period (as in Fig. 1).

Having considered the interconnection network as a linear time-invariant system the machine phase voltages $\boldsymbol{v}_m$ are given by a linear combination of the converter voltages $\boldsymbol{v}_{\mathrm{VSI}}$ and of the additional network voltages $\boldsymbol{v}_{\mathrm{NET}}$. It can be proven that, for the reciprocity property of the interconnection network, the effect of $\boldsymbol{v}_{\mathrm{NET}}$ on the machine terminal voltages $\boldsymbol{v}_m$ is weighted by the same topology-related matrix $\boldsymbol{M}$ responsible for the machine phase current constraints in (5). It results

$$\boldsymbol{v}_m = \boldsymbol{N} \cdot \boldsymbol{v}_{\mathrm{VSI}} - \boldsymbol{M} \cdot \boldsymbol{v}_{\mathrm{NET}} \tag{6}$$

where $\boldsymbol{N}$ is the $n \times n_{\mathrm{VSI}}$ matrix representing the direct effect of the converter voltages $\boldsymbol{v}_{\mathrm{VSI}}$ on the machine voltages $\boldsymbol{v}_m$. In case of star and multiple-stars connected machines (like in the configuration depicted in Fig. 1) the matrix $\boldsymbol{N}$ is simply the $n \times n$ identity matrix $\boldsymbol{I}$, while it can be different in case of other configurations (e.g., in case of open-end winding machines).

The set $\boldsymbol{v}_{\mathrm{NET}}$ behaves as an internal feedback action in a way that (5) is always satisfied. Its elements can be interpreted as voltages existing among some nodes of the system. As an example, consider the six-phase architecture represented in Fig. 1. The two isolated neutral points force the sum of the corresponding currents to be zero. The network voltages $v_{\mathrm{NET},1}$ and $v_{\mathrm{NET},2}$ in (6) can be interpreted as the potential differences between the neutral points N_1 and N_2, and the VSI reference node O, in a way that $v_{m,k} = v_{\mathrm{VSI},k} - v_{\mathrm{NET},1}$ for $k = 1, 2, 3$ and $v_{m,k} = v_{\mathrm{VSI},k} - v_{\mathrm{NET},2}$ for $k = 4, 5, 6$.

Note also that, in general, the constraints of the currents can be expressed by multiple equivalent formulations. Those formulations would lead to different constraints matrices $\boldsymbol{M}$ and also to different physical interpretations of the network voltages $\boldsymbol{v}_{\mathrm{NET}}$, but would not affect the overall model effectiveness. For example, in the same six-phase topology depicted in Fig. 1, the constraints can also be expressed as $i_{m,1} + i_{m,2} + i_{m,3} + i_{m,4} + i_{m,5} + i_{m,6} = 0$ and as $i_{m,4} + i_{m,5} + i_{m,6} = 0$. In such a case the constraints matrix would be $\boldsymbol{M} = [1\,1\,1\,1\,1\,1;\ 0\,0\,0\,1\,1\,1]^{\mathrm{T}}$, the voltage $v_{\mathrm{NET},1}$ would be the potential difference between N_1

and O, and the voltage $v_{\mathrm{NET},2}$ would be the potential difference between N_2 and N_1.

C. Combined Model

By combining (2) and (6), it results that

$$\boldsymbol{L}\cdot\frac{\mathrm{d}\boldsymbol{i}_m}{\mathrm{d}t}+\boldsymbol{R}\cdot\boldsymbol{i}_m+\ \boldsymbol{e}_{\mathrm{PM}}=\ \boldsymbol{N}\cdot\boldsymbol{v}_{\mathrm{VSI}}-\boldsymbol{M}\cdot\boldsymbol{v}_{\mathrm{NET}} \quad (7)$$

where the vector $\boldsymbol{v}_{\mathrm{NET}}$ is automatically imposed by the hardware configuration in a way that (5) is always satisfied.

For any given $n\times n_c$ constraints matrix $\boldsymbol{M}$ it is possible to compute a $n\times(n-n_c)$ configuration matrix $\boldsymbol{U}_f$ such that

$$\boldsymbol{U}_f^{\mathrm{T}}\cdot\boldsymbol{M}\ =\mathbf{0}\ \text{ and }\ \left(\boldsymbol{I}-\boldsymbol{U}_f\cdot\boldsymbol{U}_f^{\mathrm{T}}\right)\cdot\ \boldsymbol{i}_m=\mathbf{0}. \quad (8)$$

The matrix $\boldsymbol{U}_f$ can be found by computing the singular value decomposition of $\boldsymbol{M}$ and by selecting its last $(n-n_c)$ left singular vectors. This can be conveniently calculated in any numerical analysis software (e.g., MATLAB). The properties (8) of $\boldsymbol{U}_f$ are proven in Appendix A.

For example, in the six-phase machine of Fig. 1, the singular value decomposition of $\boldsymbol{M}\ =[1\,1\,1\,0\,0\,0;0\,0\,0\,1\,1\,1]^{\mathrm{T}}$ can be found in MATLAB through the command "[U,S,V] = svd(M)". The computed left singular vectors matrix $\boldsymbol{U}$ is

$$\boldsymbol{U}=\begin{bmatrix}-0.577 & 0 & -0.577 & 0.333 & 0.333 & 0.333\\ -0.577 & 0 & -0.211 & -0.455 & -0.455 & -0.455\\ -0.577 & 0 & 0.789 & 0.122 & 0.122 & 0.122\\ 0 & -0.577 & 0 & 0.667 & -0.333 & -0.333\\ 0 & -0.577 & 0 & -0.333 & 0.667 & -0.333\\ 0 & -0.577 & 0 & -0.333 & -0.333 & 0.667\end{bmatrix} \quad (9)$$

and the configuration matrix $\boldsymbol{U}_f$ is given by its last four columns.

Given (8), by premultiplying (7) by $\boldsymbol{U}_f^{\mathrm{T}}$, it results that

$$\boldsymbol{U}_f^{\mathrm{T}}\cdot\ \left(\boldsymbol{L}\cdot\frac{\mathrm{d}\boldsymbol{i}_m}{\mathrm{d}t}+\boldsymbol{R}\cdot\boldsymbol{i}_m+\boldsymbol{e}_{\mathrm{PM}}\right)=\boldsymbol{U}_f^{\mathrm{T}}\ \cdot\boldsymbol{N}\cdot\boldsymbol{v}_{\mathrm{VSI}}. \quad (10)$$

This last equation is independent of $\boldsymbol{v}_{\mathrm{NET}}$ and automatically considers the constraints (5). Naturally, when the machine currents are not subject to any constraint (e.g., each winding is supplied by a separate H-bridge, or open-end winding with connected dc buses, or when a neutral point is connected to an additional leg), and $\boldsymbol{U}_f$ is the $n\times n$ identity matrix.

III. Currents Control Algorithm

The current controller is aimed to compute the voltage references $\boldsymbol{v}^*_{\mathrm{VSI}}$ capable of driving the machine phase currents $\boldsymbol{i}_m$ towards the desired reference values $\boldsymbol{i}^*_m$. Given (10), this requirement is a multi-input multi-output control problem, which might not be easily solvable given the coupling effects and system constraints.

A. Decoupling Algorithm

The task of the decoupling algorithm is to compensate for the mutual interactions between the phase currents, which depend both on the magnetic induction and on the windings connection. The decoupling is here achieved by computing a set $\boldsymbol{v}^*_{\mathrm{VSI}}$ of converter reference voltages in a way that $\mathrm{d}\boldsymbol{i}_m/\mathrm{d}t=\boldsymbol{\delta i}^*_m$, where $\boldsymbol{\delta i}^*_m$ is a set of desired current derivatives computed from $\boldsymbol{i}^*_m$ and $\boldsymbol{i}_m$. Naturally, this problem can be solved only if both $\boldsymbol{i}^*_m$ and $\boldsymbol{\delta i}^*_m$ satisfy the constraints (5), meaning that the following identities hold [see (8) and Appendix A]:

$$\begin{cases}\boldsymbol{M}^{\mathrm{T}}\cdot\ \boldsymbol{i}^*_m=\ \mathbf{0}\\ \boldsymbol{M}^{\mathrm{T}}\cdot\ \boldsymbol{\delta i}^*_m=\ \mathbf{0}\end{cases}\Rightarrow\begin{cases}(\boldsymbol{I}-\boldsymbol{U}_f\cdot\boldsymbol{U}_f^{\mathrm{T}})\cdot\boldsymbol{i}^*_m=\ \mathbf{0}\\ (\boldsymbol{I}-\boldsymbol{U}_f\cdot\boldsymbol{U}_f^{\mathrm{T}})\cdot\ \boldsymbol{\delta i}^*_m=\ \mathbf{0}\end{cases}. \quad (11)$$

The basic idea of the proposed decoupling algorithm is to replicate the same system dynamic (10), but by replacing the phase current derivatives set $\mathrm{d}\boldsymbol{i}_m/\mathrm{d}t$ with the given reference derivative set $\boldsymbol{\delta i}^*_m$, and by replacing the VSI leg voltages set $\boldsymbol{v}_{\mathrm{VSI}}$ with the reference set $\boldsymbol{v}^*_{\mathrm{VSI}}$ to be computed. Therefore, the control problem is formalized as

$$\left(\boldsymbol{U}_f^{\mathrm{T}}\cdot\boldsymbol{N}\right)\cdot\ \boldsymbol{v}^*_{\mathrm{VSI}}=\boldsymbol{U}_f^{\mathrm{T}}\ \cdot\left(\boldsymbol{L}\cdot\boldsymbol{\delta i}^*_m+\boldsymbol{R}\cdot\boldsymbol{i}_m+\boldsymbol{e}_{\mathrm{PM}}\right). \quad (12)$$

The matrix $(\boldsymbol{U}_f^{\mathrm{T}}\cdot\boldsymbol{N})$ has dimension $(n-n_c)\times n_{\mathrm{VSI}}$ and the existence of a solution $\boldsymbol{v}^*_{\mathrm{VSI}}$ of (12) is obtained when its rank equals $(n-n_c)$. Assuming $\boldsymbol{N}$ is a full-ranked matrix with $n_{\mathrm{VSI}}\geq n$, the existence of at least one solution of (12) is guaranteed. Usually, $(\boldsymbol{U}_f^{\mathrm{T}}\cdot\boldsymbol{N})$ is not a square matrix. In that case, there is an infinite number of solutions of (12). A particular solution can be found by using the Moore–Penrose pseudoinverse operation, resulting in

$$\boldsymbol{v}^*_{\mathrm{VSI,opt}}=\left(\boldsymbol{U}_f^{\mathrm{T}}\cdot\boldsymbol{N}\right)^{\dagger}\ \cdot\boldsymbol{U}_f^{\mathrm{T}}\cdot\left(\boldsymbol{L}\cdot\boldsymbol{\delta i}^*_m+\boldsymbol{R}\cdot\boldsymbol{i}_m+\boldsymbol{e}_{\mathrm{PM}}\right). \quad (13)$$

As known, this pseudoinverse operation satisfies the condition $(\boldsymbol{U}_f^{\mathrm{T}}\cdot\boldsymbol{N})\cdot\ (\boldsymbol{U}_f^{\mathrm{T}}\cdot\boldsymbol{N})^{\dagger}=\ \boldsymbol{I}$ (i.e., it is the right pseudoinverse).

The voltage $\boldsymbol{v}^*_{\mathrm{VSI,opt}}$ provided in (13) is computed as the sum of: the desired inductive back-EMFs $(\boldsymbol{L}\cdot\boldsymbol{\delta i}^*_m)$, a compensation of the resistive voltage drops $(\boldsymbol{R}\cdot\boldsymbol{i}_m)$ and a compensation of the PM induced back-EMFs $\boldsymbol{e}_{\mathrm{PM}}$, which are all machine related terms. The weighting matrix $(\boldsymbol{U}_f^{\mathrm{T}}\cdot\boldsymbol{N})^{\dagger}\cdot\boldsymbol{U}_f^{\mathrm{T}}$ is instead only dependent on the interconnection network.

By substituting the controller (13) into the system (10) and by performing some algebraic manipulation (provided in Appendix B), it results

$$\mathrm{d}\boldsymbol{i}_m/\mathrm{d}t=\boldsymbol{\delta i}^*_m \quad (14)$$

which is the desired reference derivative seeking requirement. Since each component $\mathrm{d}i_{m,k}/\mathrm{d}t$ is only driven by the corresponding reference $\delta i^*_{m,k}$, the dynamics are decoupled.

The voltage set $\boldsymbol{v}^*_{\mathrm{VSI,opt}}$ computed with (13) usually requires some references leg voltages to be negative. Since most inverters cannot produce a negative leg voltage, the set $\boldsymbol{v}^*_{\mathrm{VSI}}$ needs to be properly conditioned to be in a given feasible range, but without affecting the derivative seeking condition (14). For a generic configuration, this can be done by adding to the optimal set $\boldsymbol{v}^*_{\mathrm{VSI,opt}}$ found as per (13) any reference set belonging to the null-space of $(\boldsymbol{U}_f^{\mathrm{T}}\cdot\boldsymbol{N})$. This operation is the generalization of the common mode voltage injection used in star-connected systems and can be formalized by using the projection operator $\boldsymbol{I}-(\boldsymbol{U}_f^{\mathrm{T}}\cdot\boldsymbol{N})^{\dagger}\cdot(\boldsymbol{U}_f^{\mathrm{T}}\cdot\boldsymbol{N})$ (which, once premultiplied by $(\boldsymbol{U}_f^{\mathrm{T}}\cdot\boldsymbol{N})$ in (10), results in a zero matrix). Then, the converter

reference voltages can be chosen as

$$\boldsymbol{v}^*_{\mathrm{VSI}} = \boldsymbol{v}^*_{\mathrm{VSI,opt}} + \left[\boldsymbol{I} - \left(\boldsymbol{U}_f^{\mathrm{T}} \cdot \boldsymbol{N}\right)^{\dagger} \cdot \left(\boldsymbol{U}_f^{\mathrm{T}} \cdot \boldsymbol{N}\right)\right] \cdot \boldsymbol{v}^*_{\mathrm{VSI,off}} \tag{15}$$

where $\boldsymbol{v}^*_{\mathrm{VSI,off}}$ is the desired offset vector. A simple and convenient choice is to set $\boldsymbol{v}^*_{\mathrm{VSI,off}}$ to the midrange values, which can be assumed by each leg (e.g., half of the total dc-bus voltage). This corresponds to what is typically done in standard carrier-based PWM algorithms. Other approaches (e.g., min–max injection) can be also studied in this framework and would lead to an offset vector $\boldsymbol{v}^*_{\mathrm{VSI,off}}$ which depends on $\boldsymbol{v}^*_{\mathrm{VSI,opt}}$.

The proposed decoupling algorithm can be easily adapted both in case of machine parameters variation and in case of windings reconfigurations. For real-time implementations, the configuration matrix $\boldsymbol{U}_f$ can be computed offline through the singular value decomposition of $\boldsymbol{M}$ (see Appendix A).

A simplification (which usually applies to star and multiple-star connected configurations) can be obtained in the special case when $\boldsymbol{N} = \boldsymbol{I}$. Indeed, in such a case, it simply results $(\boldsymbol{U}_f^{\mathrm{T}} \cdot \boldsymbol{N})^{\dagger} = (\boldsymbol{U}_f^{\mathrm{T}})^{\dagger} = \boldsymbol{U}_f$. Hence, (13) and (15) simplify to

$$\begin{aligned} \boldsymbol{v}^*_{\mathrm{VSI,opt}} &= \left(\boldsymbol{U}_f \cdot \boldsymbol{U}_f^{\mathrm{T}}\right) \cdot \left(\boldsymbol{L} \cdot \boldsymbol{\delta i}^*_m + \boldsymbol{R} \cdot \boldsymbol{i}_m + \boldsymbol{e}_{\mathrm{PM}}\right) \\ \boldsymbol{v}^*_{\mathrm{VSI}} &= \boldsymbol{v}^*_{\mathrm{VSI,opt}} + \left[\boldsymbol{I} - \left(\boldsymbol{U}_f \cdot \boldsymbol{U}_f^{\mathrm{T}}\right)\right] \cdot \boldsymbol{v}^*_{\mathrm{VSI,off}}. \end{aligned} \tag{16}$$

In this case, no pseudoinverse operation is needed and only the matrix $(\boldsymbol{U}_f \cdot \boldsymbol{U}_f^{\mathrm{T}})$ needs to be computed.

B. Decoupled Controller Design

The previously described decoupling algorithm allows meeting the condition $\mathrm{d}\boldsymbol{i}_m/\mathrm{d}t = \boldsymbol{\delta i}^*_m$, meaning that all the currents can be controlled independently from one another.

The reference $\boldsymbol{\delta i}^*_m$ can be computed with any controller which guarantees the condition $\boldsymbol{M}^{\mathrm{T}} \cdot \boldsymbol{\delta i}^*_m = \boldsymbol{0}$. A simple solution can be conveniently achieved by choosing n independent linear controllers with the same structure, each of which acts on a single-phase current by processing the seeking error $\tilde{i}_{m,k} = i^*_{m,k} - i_{m,k}$ and computing the corresponding control action $\delta i^*_{m,k}$ (with $k = 1, \ldots, n$).

By considering the ideal decoupling $\mathrm{d}i_{m,k}/\mathrm{d}t = \delta i^*_{m,k}$ provided by (14) and by modeling the discrete-time control and the converter modulation through a simple time-delay of τ (which can be approximately considered to be 1.5 times the modulation period), each phase current controller can be designed with respect to the linear system described by the same transfer function in the Laplace domain

$$\mathcal{G}(s) = \frac{\mathcal{L}\left[i_{m,k}\right](s)}{\mathcal{L}\left[\delta i^*_{m,k}\right](s)} = \frac{\mathrm{e}^{-s\tau}}{s}. \tag{17}$$

Since, in general, each steady-state current reference $i^*_{m,k}$ is a periodic function of time, it might be convenient to design the phase current controller to guarantee an infinite magnitude gain for some angular frequencies, in a way to guarantee the steady-state tracking error to be zero. By using a multiple resonances

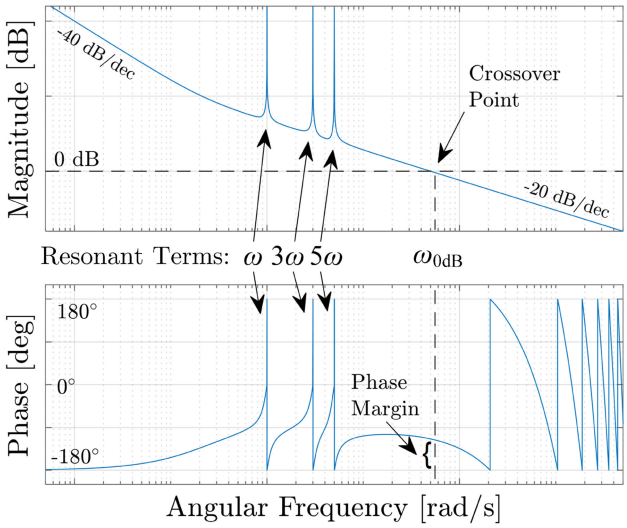

Fig. 2. Qualitative Bode diagram of the open-loop decoupled system.

structure [21], the transfer function of the controller is

$$\mathcal{C}(s) = \frac{\mathcal{L}\left[\delta i^*_{m,k}\right](s)}{\mathcal{L}\left[\tilde{i}_{m,k}\right](s)} = K_P + \frac{K_I}{s} + \sum_{h=1}^{n_{res}} K_{R,h} \cdot \frac{s \cdot \omega_h}{s^2 + \omega_h^2}. \tag{18}$$

Each resonance frequency ω_h should be properly tuned with the angular speed of the machine ω. It is convenient to choose the resonance frequencies ω_h of the decoupled controller transfer function (18) to be multiple integers of $P_p \cdot \omega$ (P_p being the pole pairs). The resonant actions can also compensate for the steady-state effects of imperfect knowledge of the machine parameters in the decoupling algorithm (13) and the effects of unmodeled phenomena (e.g., iron saturation) [22], [23].

A qualitative Bode diagram of the open-loop frequency response of the system is provided in Fig. 2, where three resonant terms have been included to compensate for the fundamental, the third and the fifth current harmonic components. As for any linear control, the 0 dB crossover frequency $\omega_{0\ \mathrm{dB}}$ is to be chosen as a tradeoff between the closed-loop controller dynamic requirements and its robustness. Indeed, given the phase delay caused by (17), high crossover frequencies may lead to low values for the stability phase margin. It can also be deduced that the slower is the rotor speed ω, the higher is the number of resonant terms, which can be used in (18) while still guaranteeing the asymptotic stability of the closed-loop control.

Finally, to always meet the requirement $\boldsymbol{M}^{\mathrm{T}} \cdot \boldsymbol{\delta i}^*_m = \boldsymbol{0}$ (regardless of some possible references computation mistakes or of undesirable effects of current measurement noises), it is convenient to premultiply both $\boldsymbol{i}_m$ and $\boldsymbol{i}^*_m$ by $(\boldsymbol{U}_f \cdot \boldsymbol{U}_f^{\mathrm{T}})$.

IV. Reference Currents Computation Strategy

The machine control strategy is aimed to supply a desired electromagnetic torque T^*_{em} through a proper choice of the phase reference currents $\boldsymbol{i}_m$. Considering the n_c current constraints expressed by (5) and the torque development requirement formalized as per (4), there are $n - (n_c + 1)$ degrees of freedom,

which can be properly exploited to optimize some system performances. An MTPA strategy can be conveniently formalized to develop the desired torque while minimizing the required currents. In this context, the proposed objective function is an equivalent root mean square (rms) current for the whole machine, chosen as

$$I_{\mathrm{RMS}} = \sqrt{\boldsymbol{i}_m^{\mathrm{T}} \cdot \boldsymbol{i}_m} \quad = \quad \sqrt{\sum_{k=1}^{n} i_{m,k}^2}. \tag{19}$$

Under a reasonable hypothesis that all the machine windings have the same resistance, the minimization of I_{RMS} leads to the minimization of the machine stator copper losses.

The MTPA strategy can be analytically formalized as the constrained optimization problem

$$\min_{\boldsymbol{i}_m} \left\{ \boldsymbol{i}_m^{\mathrm{T}} \cdot \boldsymbol{i}_m \right\} \text{subject to} \begin{cases} \boldsymbol{f}_{\mathrm{PM}}^{\mathrm{T}} \cdot \ \boldsymbol{i}_m = T_{em}^* \\ \boldsymbol{M}^{\mathrm{T}} \cdot \ \boldsymbol{i}_m = \boldsymbol{0}. \end{cases} \tag{20}$$

where it is worth recalling that $\boldsymbol{f}_{\mathrm{PM}}$ periodically depends on the rotor position θ. The optimization problem (20) extends the procedure presented in [17] and [19] to a generic winding configuration. It is worth noting that, similarly to (12), also (20) could be solved with a pseudoinverse algorithm. However, since $\boldsymbol{f}_{\mathrm{PM}}$ is not constant, the required pseudoinverse matrix would be dependent on θ and could not be computed offline. Therefore, an analytical solution of (20), suitable for real-time applications, is here derived by using Lagrange's multiplier method.

A Lagrangian function for (20) can be formed as

$$\mathfrak{L} \ = \boldsymbol{i}_m^{\mathrm{T}} \ \cdot \boldsymbol{i}_m - \mu \cdot \left(\boldsymbol{f}_{\mathrm{PM}}^{\mathrm{T}} \cdot \boldsymbol{i}_m - T_{em}^* \right) - \boldsymbol{\nu}^{\mathrm{T}} \cdot \left(\boldsymbol{M}^{\mathrm{T}} \cdot \boldsymbol{i}_m \right) \tag{21}$$

where μ is the multiplier related to the torque development requirement, while $\boldsymbol{\nu}$ is a $n_c \times 1$ vector of multipliers related to the n_c algebraic constraints expressed by (5). The optimal solution is then found by nullifying the gradient of $\mathfrak{L}(\boldsymbol{i}_m, \mu, \boldsymbol{\nu})$, leading to the linear algebraic system

$$\begin{aligned} \partial\mathfrak{L}/\partial\boldsymbol{i}_m &= \ 2 \cdot \boldsymbol{i}_m - \mu \cdot \boldsymbol{f}_{\mathrm{PM}} - \boldsymbol{M} \cdot \boldsymbol{\nu} \ = \boldsymbol{0} \\ \partial\mathfrak{L}/\partial\mu \ &= \ \boldsymbol{f}_{\mathrm{PM}}^{\mathrm{T}} \cdot \boldsymbol{i}_m - \ T_{em}^* = 0 \\ \partial\mathfrak{L}/\partial\boldsymbol{\nu} \ &= \ \boldsymbol{M}^{\mathrm{T}} \cdot \ \boldsymbol{i}_m = \boldsymbol{0} \end{aligned} \tag{22}$$

The solution of (22) provides the optimal currents set

$$\boldsymbol{i}_m^* = \frac{\boldsymbol{W} \cdot \boldsymbol{f}_{\mathrm{PM}}}{\boldsymbol{f}_{\mathrm{PM}}^{\mathrm{T}} \cdot \boldsymbol{W} \cdot \boldsymbol{f}_{\mathrm{PM}}} \cdot T_{em}^* \tag{23}$$

where the weighting matrix $\boldsymbol{W}$ (which only depends on the algebraic constraints imposed on the currents) is defined as

$$\boldsymbol{W} \ = \ \boldsymbol{I} - \boldsymbol{M} \cdot \left(\boldsymbol{M}^{\mathrm{T}} \cdot \boldsymbol{M} \right)^{-1} \cdot \boldsymbol{M}^{\mathrm{T}}. \tag{24}$$

In absence of any current constraint, it simply results $\boldsymbol{W} \ = \ \boldsymbol{I}$.

Since (23) is the only solution to the system (22) and the objective function (19) is convex, it is the global minimum for the optimization problem (20).

As expected, the optimal phase currents set (23) is proportional to the reference electromagnetic torque T_{em}^* and periodically depends on θ through the values assumed by $\boldsymbol{f}_{\mathrm{PM}}$.

It can be proven that, for machines with sinusoidal back-EMFs in symmetrical or multiple three-phase winding configuration, the denominator of (23) is constant and, hence, the optimal current references are sinusoidal functions of θ. On the contrary, for asymmetrical winding configurations and/or nonsinusoidal back-EMFs, the optimal currents are generally nonsinusoidal functions of the rotor position θ. This also applies to postfault machine configurations.

Some problems may arise when $\boldsymbol{f}_{\mathrm{PM}}^{\mathrm{T}} \cdot \boldsymbol{W} \cdot \boldsymbol{f}_{\mathrm{PM}}$ is close to zero. Indeed, the computed reference currents would tend to infinity and be unfeasible for real applications. This condition means that the machine is unable to supply the desired torque while satisfying the hardware constraints. For example, this happens when the stator currents are not capable of generating a rotating magnetic field at the machine air-gap. Thanks to the high number of phases, this hardly happens in multiphase drives and can almost always be disregarded.

It is worth emphasizing that, by simply partitioning $\boldsymbol{i}_m^*$ and $\boldsymbol{f}_{\mathrm{PM}}$, the strategy (20) can be also applied to a chosen winding subset to control the torque developed by the corresponding currents. This property can be exploited for torque sharing purposes and, especially in case of different windings subsets supplied by independent sources, it can be conveniently used to transfer power between the different subsets. This capability extends the independent torque control of machines with a modular configuration of the stator winding [10], [11] and, as exemplified in Section VII-E, it can even be applied in presence of open-circuit faults.

V. Control Scheme

A schematic representation of the proposed control algorithm is depicted in Fig. 3.

First, the "speed controller" compares the reference speed ω^* with the machine speed ω and computes the reference electromagnetic torque T_{em}^* to be applied. Similarly to any standard electrical drive, the controller can be a linear regulator with transfer function $\mathcal{C}_\omega(s)$, like a PI.

Next, the "back-EMFs estimation" block is executed to compute the normalized back-EMFs vector $\boldsymbol{f}_{\mathrm{PM}}$ (necessary for the current references computation strategy) and to estimate the PM induced voltages $\boldsymbol{e}_{\mathrm{PM}} = \ \omega \cdot \boldsymbol{f}_{\mathrm{PM}}$ (to be compensated in the feedback current control algorithm).

The "MTPA strategy" block is then executed to compute the reference currents set $\boldsymbol{i}_m^*$ via (23). In case of torque sharing strategies, the block is separately executed for the chosen winding subsets (i.e., by properly partitioning $\boldsymbol{f}_{\mathrm{PM}}$ into different subsets $\boldsymbol{f}_{\mathrm{PM,SET}k}$ and using the corresponding weighting matrices $\boldsymbol{W}_{\mathrm{SET}k}$ for each kth subset).

Finally, the "current controller" is executed to properly drive the set $\boldsymbol{i}_m$ towards $\boldsymbol{i}_m^*$. The resulting reference voltage set $\boldsymbol{v}_{\mathrm{VSI}}^*$ is finally supplied to the converter pulse width modulator to find the switching signals for the semiconductor devices.

Any change in the system configuration or parameters only requires the update of the control matrices, thus requiring a minimal controller reconfiguration. Moreover, all the control matrices can be also conveniently computed offline or during an

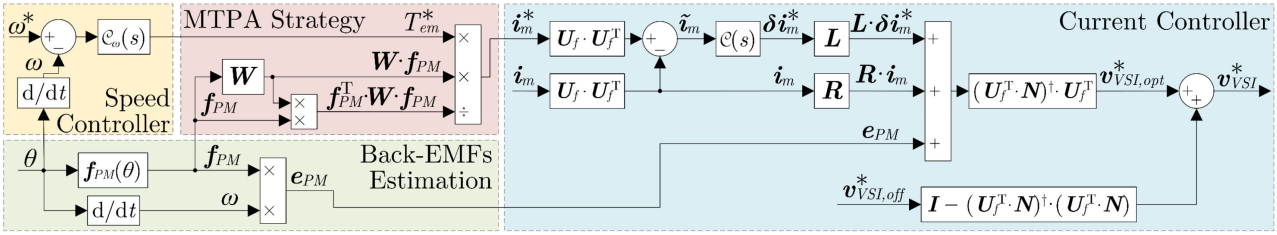

Fig. 3. Functional scheme of the proposed controller.

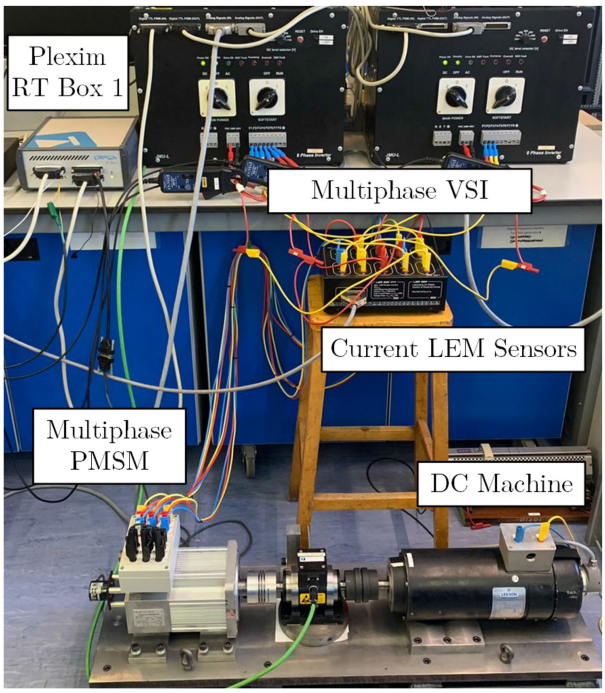

Fig. 4. Experimental setup.

algorithm initialization routine to reduce the required computational effort for real-time applications.

VI. Experimental Setup Description

The experimental setup used to validate the proposed control algorithm is depicted in Fig. 4.

The controlled machine is a nine-phase PMSM with three pole pairs. Its windings have been designed as three symmetrical three-phase sets whose magnetic axes are mutually shifted by 15° in the electrical reference frame (i.e., 5° mechanically). It is, therefore, possible to define the machine magnetic axes angles set $\boldsymbol{\alpha} = [0^\circ\ 120^\circ\ 240^\circ\ 15^\circ\ 135^\circ\ 255^\circ\ 30^\circ\ 150^\circ\ 270^\circ]^{\mathrm{T}}$. All the 18 winding terminals (the positive/negative couples for all $n = 9$ machine phases) are available externally. The PMSM shaft is coupled to a dc machine used for loading. The total drive inertia has been estimated to be around $8 \cdot 10^{-3}$ kg $\cdot$ m^2.

The PM induced back-EMFs have been found by measuring the terminal voltages when the machine was spinning (run by the dc machine) and all the winding terminals were disconnected. All the back-EMFs are sinusoidal functions of the electrical rotor position 3θ and are shifted from each other according to their magnetic axis angles. Therefore, the PM induced fluxes and the corresponding normalized back-EMFs can be, respectively, modeled as

$$\begin{aligned} \lambda_{\mathrm{PM},k}\ (\theta) &= \Lambda_{\mathrm{PM},k} \cdot \cos(3\theta - \alpha_k) \\ f_{\mathrm{PM},k}\ (\theta) &= \partial\lambda_{\mathrm{PM},k}/\partial\theta\ =\ -3 \cdot \Lambda_{\mathrm{PM},k} \cdot \sin(3\theta - \alpha_k)\,. \end{aligned} \tag{25}$$

The flux magnitudes $\Lambda_{\mathrm{PM},k}$ are reported in Table I and it can be noted that they are equal for the phases belonging to the same symmetrical three-phase set, but are lower for the set {4,5,6}.

All the windings have approximately the same resistance $R \approx 8\ \Omega$ (measured by dc), meaning that the resistances matrix can be modeled as a scalar matrix $\boldsymbol{R} = R \cdot \boldsymbol{I}$.

The machine inductances matrix elements $L_{k1,k2}$ have been found at blocked rotor by separately supplying each k_1th machine phase with a 50 Hz voltage $v_{m,k1}$ and measuring the corresponding current $i_{m,k1}$ and the induced voltage $v_{m,k2}$ in all the other windings (left in open-circuit). The results are reported in Table II and it can be verified that, coherently with the mathematical model, $\boldsymbol{L}$ is symmetric and positive definite.

Additional information about this machine, like the dq parameters and the windings diagram, can be found in [10]. The machine has been supplied using two custom-made multiphase inverters, based on Infineon FS50R12KE3 IGBT modules. The $n_{\mathrm{VSI}} = 9$ inverter legs have a common dc-bus, whose voltage is

TABLE I
PM Induced Flux Magnitudes [mWb]

k	1	2	3	4	5	6	7	8	9
$\Lambda_{PM,k}$	268	268	268	259	259	259	268	268	268

TABLE II
Inductances Matrix Parameters [mH]

$L_{k1,k2}$	1	2	3	4	5	6	7	8	9
1	25.2	–3.3	–3.3	13.9	–6.2	–2.1	8.3	–7.3	0.4
2	–3.3	25.2	–3.3	–2.1	13.9	–6.2	0.4	8.3	–7.3
3	–3.3	–3.3	25.2	–6.2	–2.1	13.9	–7.3	0.4	8.3
4	13.9	–2.1	–6.2	17.2	–3.3	–3.3	13.9	–6.2	–2.1
5	–6.2	13.9	–2.1	–3.3	17.2	–3.3	–2.1	13.9	–6.2
6	–2.1	–6.2	13.9	–3.3	–3.3	17.2	–6.2	–2.1	13.9
7	8.3	0.4	–7.3	13.9	–2.1	–6.2	25.2	–3.3	–3.3
8	–7.3	8.3	0.4	–6.2	13.9	–2.1	–3.3	25.2	–3.3
9	0.4	–7.3	8.3	–2.1	–6.2	13.9	–3.3	–3.3	25.2

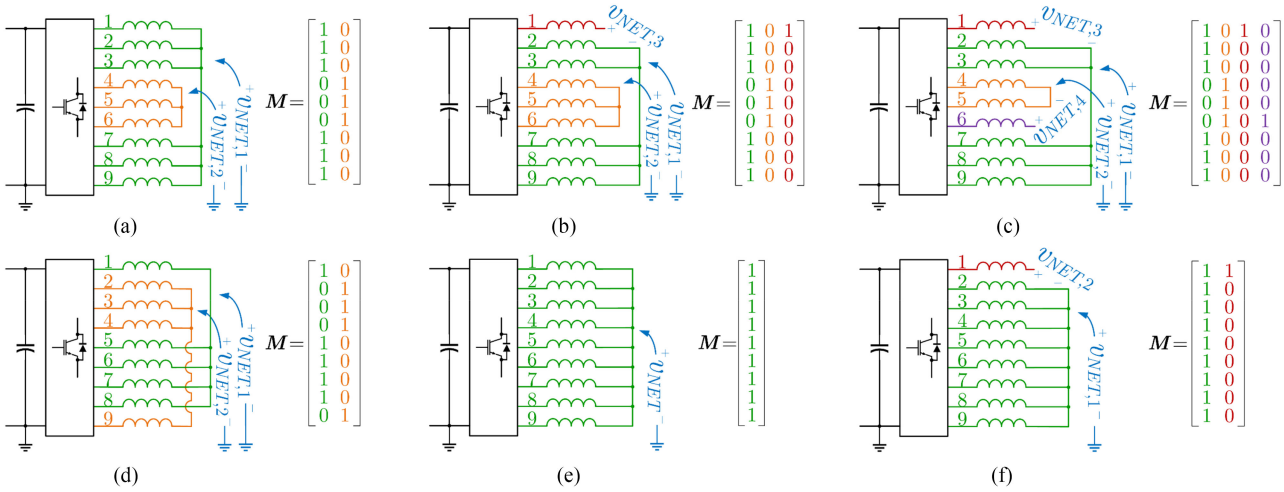

Fig. 5. Schematic representation, constraints matrix $\boldsymbol{M}$ and network voltages $v_{\mathrm{NET},k}$ for the different windings connections used in the experimental tests.

equal to 200 V and is supplied by a Sorensen SGI600/25 single quadrant dc-voltage source.

The positive terminals of the PMSM are connected to the output terminals of the VSI, meaning that the configuration network matrix $\boldsymbol{N}$ in (6) is a 9×9 identity matrix. On the contrary, the winding negative terminals are connected differently for each of the testing scenarios described in the following sections. Therefore, the constraints matrix $\boldsymbol{M}$ is not always the same. Fig. 5 shows a schematic representation of the different windings connections implemented in the experimental tests, together with the corresponding constraints matrices $\boldsymbol{M}$. The figure also shows the physical interpretation of the network voltages $v_{\mathrm{NET},k}$ (with $k = 1, \ldots, n_c$) corresponding to the chosen constraints matrices $\boldsymbol{M}$.

The control algorithm has been implemented with a Plexim RT Box 1 platform. All nine phase currents are measured through LEM sensors and the machine position and angular speed are provided by an incremental encoder (Omron E6B2-CWZ1X, with resolution of 1000 pulses/revolution).

The control algorithm is executed with a 10 kHz sampling rate. A PI controller has been used to compute the reference torque T^*_{em} needed to regulate the machine angular speed ω towards the desired reference speed ω^*. The reference torque T^*_{em} has been limited to a maximum value of 5 Nm. For each testing scenario, both the configuration matrices $\boldsymbol{U}_f$ and the MTPA weighing matrix $\boldsymbol{W}$ have been computed offline with a proper initialization routine. Since $\boldsymbol{N} = \boldsymbol{I}$, the current control algorithm does not require any pseudoinverse matrix computation and simplifies to the one described in (16). The feedback current controller transfer function $\mathcal{C}(s)$ in (18) has been designed with a proportional action, an integral action and six resonant actions synchronized with the lowest odd integer multiples of the electrical angular speed 3ω (i.e., $\omega_h = h \cdot 3\omega$, with $h = 1,3,5,7,9,11$). Finally, the offset vector $\boldsymbol{v}^*_{\mathrm{VSI,off}}$ in (16) has been set to half of the total dc-bus voltage for all the legs. A standard triangular carrier-based pulsewidth-modulation technique has been implemented to operate the converter, resulting in a switching frequency of 10 kHz.

VII. Experimental Results

To highlight the generality of the proposed approach, it has been tested in several different scenarios, described and discussed in the following sections.

A. Healthy Configuration

This testing scenario is aimed at showing the effectiveness of the proposed control in a healthy machine configuration, both at varying speed and at varying load. The test has been conducted as follows. Initially, the machine works at no load at the speed of $-500\,\mathrm{r/min}$ and the electromagnetic torque only needs to balance the mechanical friction. Then, the machine reference speed is changed to $500\,\mathrm{r/min}$. After the speed inversion has been performed and the machine has reached the steady-state conditions, the mechanical load is changed to the final value of about 2.3 Nm by commanding (via RT Box) the closing of a contactor, which connects an external resistor to the armature terminals of the dc machine.

The configuration under analysis is represented in Fig. 5(a). The machine windings are divided into two star-connected groups with two isolated neutral points. The first group includes the windings {1,2,3,7,8,9} and, given the machine design, behaves as an equivalent six-phase machine (with two symmetrical three-phase windings sets mutually shifted by 30°). The second group includes the remaining windings {4,5,6} and is equivalent to a symmetrical three-phase machine. Given the symmetrical and sinusoidal configuration, all the current references are sinusoidal functions of the electrical rotor position 3θ.

The results are depicted in Fig. 6. The first three subplots show the machine currents (solid lines) and the corresponding references (dashed lines). The fourth subplot shows the developed electromagnetic torque T_{em} (solid line) and the reference T^*_{em} (dashed line). The developed torque has been estimated by computing (4) with the measured currents. The last subplot shows the machine speed ω (solid line) and its reference value ω^* (dashed line); a zoomed version of the speed dynamics after the load torque step change is shown in a box inside the same subplot.

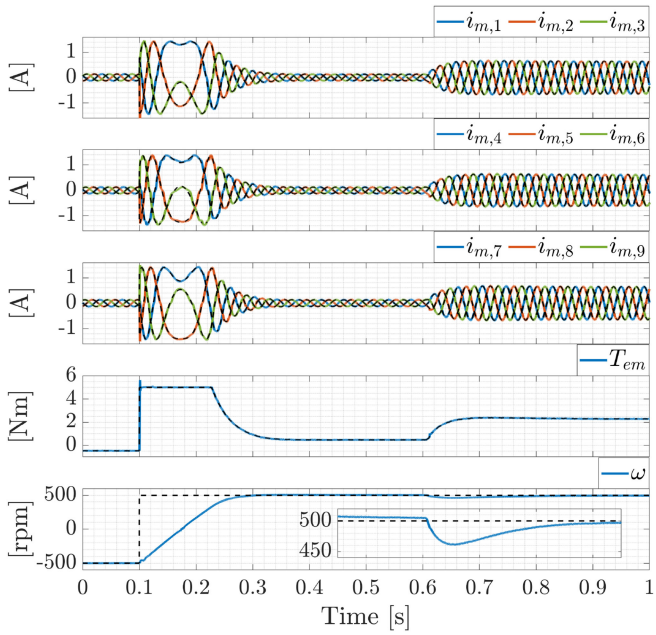

Fig. 6. Experimental results in the healthy configuration test.

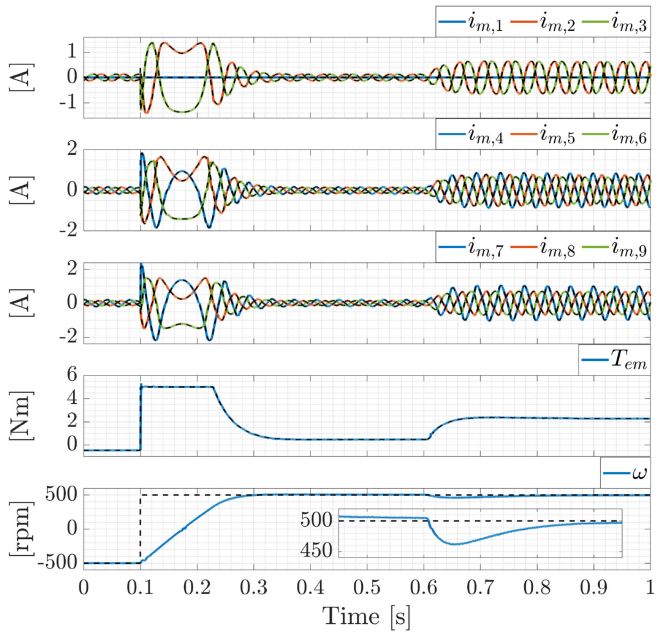

Fig. 7. Experimental results in the post-fault configuration test (phase 1 open).

For the first 100 ms the machine is in steady-state condition at $-500\,\mathrm{r/min}$. The currents are sinusoidal and develop torque of around -0.5 Nm to neutralize the overall drive train friction. Immediately after the speed reference change, the torque reference jumps to the maximum value of 5 Nm and the reference currents increase accordingly (coherently with the MTPA strategy). When the machine speed approaches its reference value, the torque decreases down to the final value of around 0.5 Nm (which is again only related to the drive train friction). The speed inversion is completed in around 250 ms and the steady-state currents are again sinusoidal functions of time, but their phase displacement is reversed (e.g., initially $i_{m,2}$ was ahead of $i_{m,1}$, while now it is opposite). At around 600 ms the controlled contactor is closed, and the dc machine terminals are connected to the external resistor. The drive loading torque increases and the speed drops down from the reference value. Then, to counteract this drop, the speed controller increases the reference torque T^*_{em} and, because of the MTPA strategy, the PMSM current references $i^*_{m,k}$ (with $k = 1, \ldots, 9$) also increase proportionally to it. The speed reaches the minimum value of around $460\,\mathrm{r/min}$ after 50 ms and is regulated back to the reference value of $500\,\mathrm{r/min}$ in around 350 ms. At steady-state conditions, the currents are again sinusoidal in time and develop an overall electromagnetic torque of around 2.3 Nm.

B. Postfault Configuration

This experiment is aimed at showing how the proposed control algorithm performs in a postfault configuration. The testing scenario is the same as in the previous case study.

The winding configuration, schematically represented in Fig. 5(b), is modified with respect to the previous case study by physically disconnecting phase 1 of the machine. The only difference in the control algorithm is related to the configuration matrix $\boldsymbol{U}_f$ and to the MTPA weighting matrix $\boldsymbol{W}$, which are now computed with the modified constraints matrix $\boldsymbol{M}$ shown in Fig. 5(b). The additional column of $\boldsymbol{M}$ identifies the open-circuit constraint $i_{m,1} = 0$.

The results are depicted in Fig. 7. If compared with the healthy configuration scenario, both the speed and the torque responses are the same, while the current waveforms are different. The opening of phase 1 makes the windings configuration asymmetrical, resulting in a nonconstant denominator of (23). The reference currents computed through the MTPA strategy are not anymore sinusoidal functions of 3θ and the steady-state currents are not sinusoidal in time either. They can still be perfectly tracked thanks to the resonant actions included in the decoupled current controller.

The magnitude of the currents is however higher than in the healthy configuration. It has been computed that, in steady state condition, the overall rms current I_{RMS} in this faulty scenario is (on average in a full rotor cycle) around 9% higher than in the healthy configuration. This behavior is expected, because the faulty machine is asked to develop the same electromagnetic torque of the healthy configuration while satisfying more constraints on the phase currents (i.e., $i_{m,1} = 0$).

The same strategy also applies in case that more than one fault is present. Fig. 8 shows the results under the same testing scenario in case of an additional fault on phase 6 of the machine [i.e., it refers to the configuration of Fig. 5(c)]. Again, the speed and torque response are the same, while the currents are different. In this case, given the additional constraint $i_{m,6} = 0$, the machine steady state rms current I_{RMS} is around 19% higher than in the healthy configuration.

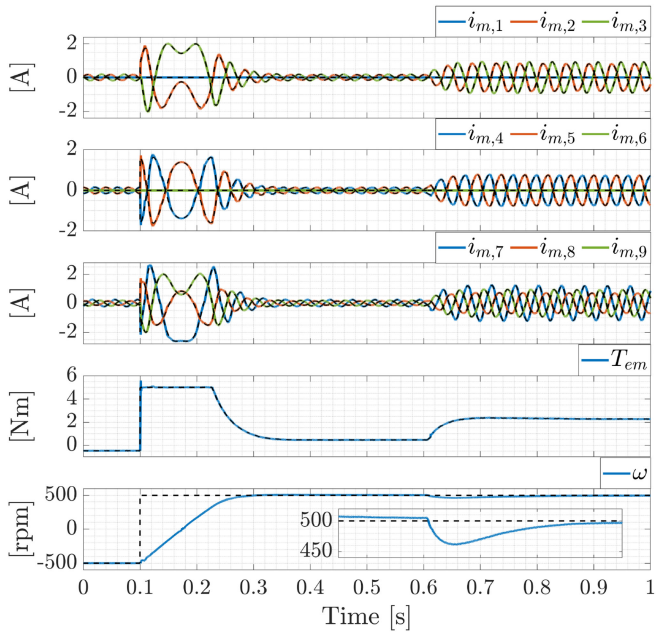

Fig. 8. Experimental results in the post-fault configuration test (phase 1 and phase 6 open).

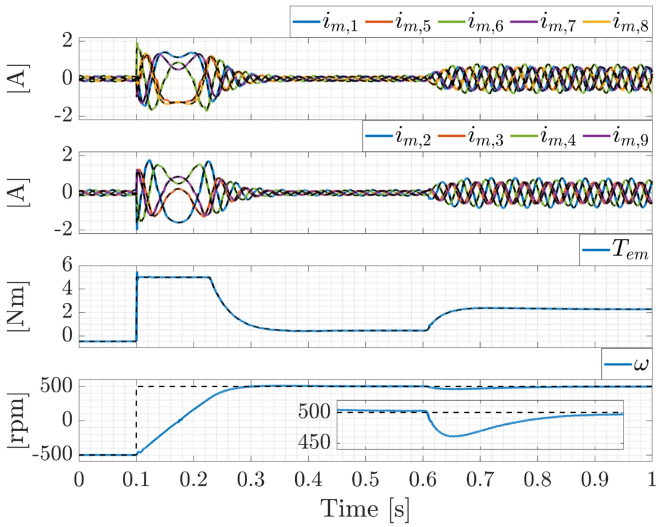

Fig. 9. Experimental results in the highly asymmetrical configuration test.

C. Highly Asymmetrical Configuration

This testing scenario, by considering an unrealistic machine configuration, is aimed at emphasizing the generality of the proposed approach. The machine windings are now divided into two star-connected groups with isolated neutral points. The first group is realized with the five-phase set {1,5,6,7,8}, while the second group is realized with the remaining four-phase set {2,3,4,9}. The windings layout and the corresponding constraints matrix $\boldsymbol{M}$ are given in Fig. 5(d). The testing scenario is the same as in the previous cases.

The results are given in Fig. 9. Again, both the speed and the torque responses are the same as in the previous cases, while the currents are different. Similarly to the postfault configuration scenario, the asymmetrical configuration of the machine windings makes the reference currents nonsinusoidal. However, the combined effect of the decoupling algorithm and of the resonant controller actions performs in a satisfactory way and allows the currents to be controlled even in such an uncommon winding configuration.

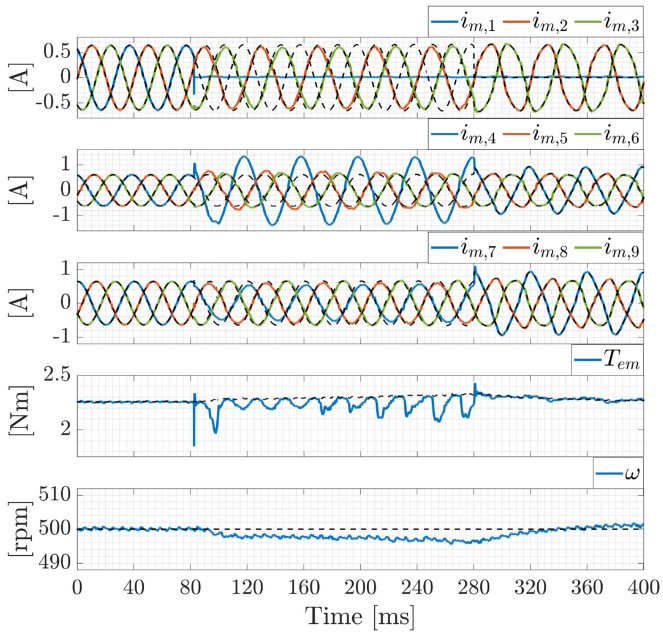

Fig. 10. Experimental results in the real-time post-fault reconfiguration test.

D. Real-Time Postfault Reconfiguration

This scenario is aimed at showing the fundamental role of the configuration matrix $\boldsymbol{U}_f$ selection on the feedback current control. This is obtained by emulating an open-winding fault event and the real-time controller reconfiguration.

Initially, the machine windings are star connected with a single isolated neutral point [as in Fig. 5(e)]. After 80 ms, the winding 1 of the machine is physically disconnected by commanding (via RT Box) the opening of a serially-connected contactor [i.e., the windings layout changes to the one depicted in Fig. 5(f)]. The structure of the controller is kept unaltered for another 200 ms [i.e., it still refers to the healthy condition of Fig. 5(e)] and is finally adapted to the postfault condition by considering the correct constraints matrix $\boldsymbol{M}$ of Fig. 5(f) (and using the corresponding $\boldsymbol{U}_f$ and $\boldsymbol{W}$ matrices). For the whole test the machine is kept at an angular speed of 500 r/min and is subjected to a mechanical load of around 2.3 Nm applied to the motor shaft by the dc machine.

The results are depicted in Fig. 10. During the first 80 ms, all the machine currents follow the corresponding sinusoidal references. Then $i_{m,1}$ is forced to zero (via hardware) without altering the controller structure. The current references (dashed traces) are still sinusoidal waveforms, but the measured currents are unable to follow them (which is expected because the references are not compatible with the new system configuration). This effect is particularly evident in the current $i_{m,4}$, which is

severely increased with respect to the others. Since the currents cannot follow their references, also the developed torque T_{em} cannot follow the desired value T^*_{em} and periodically oscillates between 2 Nm and 2.3 Nm. The decrease of the average torque also leads to a reduction of the machine's angular speed.

At time $t = 280$ ms the controller structure is finally updated. Coherently with the updated (i.e., faulty) structure, the reference current $i^*_{m,1}$ is kept at zero, while all the other current references become nonsinusoidal (which again is expected, given the asymmetrical structure of the postfault machine configuration). The measured currents are quickly and effectively driven towards the corresponding references, the electromagnetic torque can again follow T^*_{em} and the speed is slowly kept back to $\omega^* = 500$ r/min.

E. Torque Sharing

This testing scenario is aimed at showing the torque sharing capabilities of the proposed references computation strategy.

In this case, the machine windings are divided into two independent subsets. The first winding subset aim is to keep the machine's angular speed at the reference value of 500 r/min ("motoring" mode), while the second winding subset aim is to develop a desired braking torque $T^*_{em,br}$ ("braking" mode). Initially the braking torque is 0 Nm; then it is changed to 2 Nm. In such a way, it is possible to transfer power from the motoring set to the braking set. For the whole test the machine is loaded with an external torque of around 0.5 Nm.

The experiment is here done for the healthy windings configuration represented in Fig. 5(a). The machine windings are divided into two star-connected groups with two isolated neutral points. The motoring subset includes the windings {1,2,3,7,8,9} and the braking subset the windings {4,5,6}.

The currents references are found by separately applying the MTPA strategy (23) to the two subsets. To be more specific, the references $\boldsymbol{i}^*_{m,\mathrm{SET1}} = [i^*_{m,1}, i^*_{m,2}, i^*_{m,3}, i^*_{m,7}, i^*_{m,8}, i^*_{m,9}]^{\mathrm{T}}$ of the six-phase motoring set are found by applying (23) with respect to the reference torque $T^*_{em,\mathrm{SET1}} = T^*_{em} + T^*_{em,br}$ and to the six-phase normalized back-EMFs vector $\boldsymbol{f}_{\mathrm{PM,SET1}} = [f_{\mathrm{PM},1}, f_{\mathrm{PM},2}, f_{\mathrm{PM},3}, f_{\mathrm{PM},7}, f_{\mathrm{PM},8}, f_{\mathrm{PM},9}]^{\mathrm{T}}$. The weighting matrix $\boldsymbol{W}_{\mathrm{SET1}}$ is computed via (24) with the constraints matrix $\boldsymbol{M}_{\mathrm{SET1}} = [1\,1\,1\,1\,1\,1]^{\mathrm{T}}$ (which identifies the isolated neutral point constraint of the six-phase group). Similarly, the references $\boldsymbol{i}^*_{m,\mathrm{SET2}} = [i^*_{m,4}, i^*_{m,5}, i^*_{m,6}]^{\mathrm{T}}$ of the three-phase braking set are found by applying (23) with respect to the torque $T^*_{em,\mathrm{SET2}} = -T^*_{em,br}$ and to the three-phase normalized back-EMFs set $\boldsymbol{f}_{\mathrm{PM,SET2}} = [f_{\mathrm{PM},4}, f_{\mathrm{PM},5}, f_{\mathrm{PM},6}]^{\mathrm{T}}$. Its weighting matrix $\boldsymbol{W}_{\mathrm{SET2}}$ is computed via (24) with a constraints matrix $\boldsymbol{M}_{\mathrm{SET2}} = [1\,1\,1]^{\mathrm{T}}$ (which identifies the isolated neutral point constraint of the three-phase group).

Note that, despite the different current references computation strategy, the current control algorithm of this testing scenario is equal to the one described in Section VII-A (i.e., the control matrices $\boldsymbol{M}$ and $\boldsymbol{U}_f$ are the same).

Fig. 11 shows the experimental results of this scenario. For the first 80 ms the braking torque $T^*_{em,br}$ is 0 Nm and then it is changed to 2 Nm.

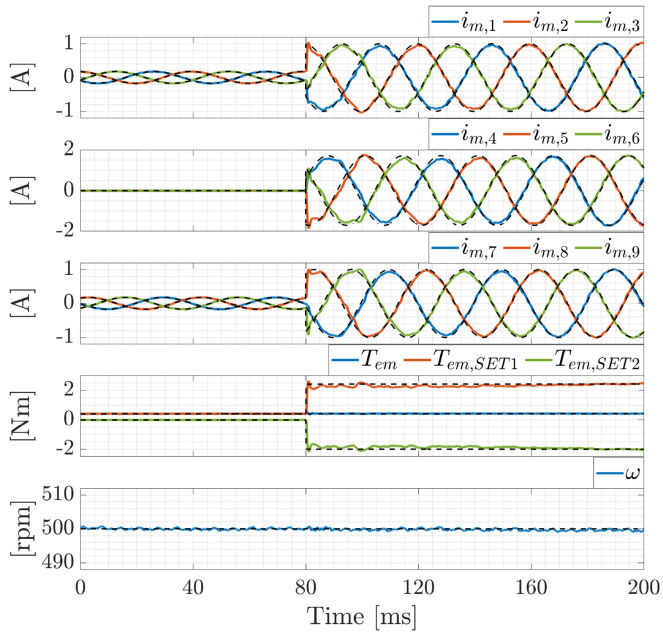

Fig. 11. Experimental results in the torque sharing test (healthy machine).

By observing the machine phase currents it can be noted that, since for the first 80 ms the three-phase set is asked not to produce any torque, the corresponding currents are zero. The six-phase set currents (which are sinusoidal and with the same magnitude) only need to balance the mechanical loading torque.

After the braking torque $T^*_{em,br}$ is changed to 2 Nm, the currents of the three-phase braking set increase to follow the corresponding references which, given the symmetrical configuration of the three-phase braking set, are also sinusoidal waveforms. To balance the braking torque, the currents of the six-phase motoring set also increase their magnitude around 5 times (i.e., they now need to develop a motoring torque of 2.5 Nm against the initial value of 0.5 Nm related to the sole mechanical load). After an initial transient, all the currents can perfectly track their references.

The fourth subplot of Fig. 11 shows the overall torque T_{em} and the torques developed by the two winding subsets $T_{em,\mathrm{SET1}}$ and $T_{em,\mathrm{SET2}}$, which have been estimated by computing the analytical expression (4) and by only selecting the phase indexes related to the two subsets. As can be noted, after an initial transient, $T_{em,\mathrm{SET2}}$ reaches the desired value of -2 Nm and $T_{em,\mathrm{SET1}}$ the corresponding value of 2.5 Nm. The overall torque developed at the shaft, which is given by the combined contribution of the two subsets, is almost unaffected by the currents transient and is kept to the constant value of 0.5 Nm required by the mechanical load.

As can be seen in the last subplot of Fig. 11, the machine speed ω is unaffected by the change of the braking torque and is kept at its reference value $\omega^* = 500$ r/min.

The same torque-sharing strategy can be also applied to a faulty configuration. This is here exemplified by repeating the same testing scenario for the faulty configuration represented in Fig. 5(b), in which phase 1 has been physically disconnected. Now, the currents control algorithm is the same as

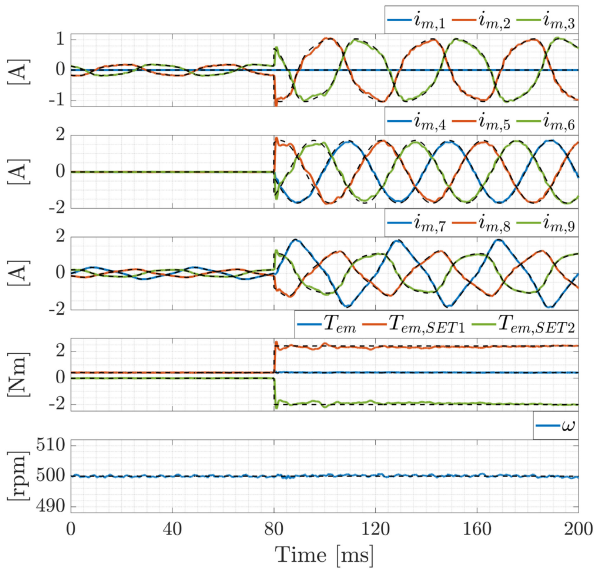

Fig. 12. Experimental results in the torque sharing test (faulty machine).

for the first postfault configuration examined in Section VII-B, while the only difference in the references computation strategy is that the motoring subset weighting matrix $\boldsymbol{W}_{\mathrm{SET1}}$ is this time computed via (24) with the modified constraints matrix $\boldsymbol{M}_{\mathrm{SET1}} = [1\,1\,1\,1\,1\,1; 1\,0\,0\,0\,0\,0]^{\mathrm{T}}$, which now also includes the additional constraint $i_{m,1} = 0$.

Fig. 12 shows the experimental results. Again, the currents of the three-phase braking set are initially zero (because the reference braking torque is 0 Nm) and then, after the settling transient, they follow the same sinusoidal reference of the previous case study (because the three-phase set is not affected by the fault). On the contrary, the currents of the motoring subset are not sinusoidal anymore, because of the asymmetrical winding configuration following the postfault reconnection (i.e., the term $\boldsymbol{f}^{\mathrm{T}}_{\mathrm{PM,SET1}} \cdot \boldsymbol{W}_{\mathrm{SET1}} \cdot \boldsymbol{f}_{\mathrm{PM,SET1}}$ is not constant). These currents show the same waveforms both before and after the reference braking torque change, but their magnitude increases about 5 times because of the corresponding increase of the reference torque $T^{*}_{em,\mathrm{SET1}}$. Once again, after an initial transient, the electromagnetic torques developed by the two sets follow their respective references, while the overall machine torque T_{em} and the mechanical speed ω are almost unaffected.

VIII. Conclusion

This article presents a generalized approach for the modeling and control of a multiphase surface-mounted PMSM drive.

The mathematical model is written in the phase variables domain, it is generalized with respect to the system configuration and parameters, and explicitly takes into account the algebraic constraints on the machine phase currents.

The proposed current controller is also completely designed in the phase variables domain and does not require any VSD or rotational transformation. It is based on a pseudoinverse decoupling algorithm, which, coherently with the system constraints, allows to independently drive all the phase currents with any standard linear single-input/single-output control algorithm. Since the steady-state currents are periodic functions of time, to guarantee a zero steady-state tracking error, the chosen decoupled controller is composed of a proportional action, an integral action and several resonant actions synchronized with the angular speed of the machine.

The proposed current references computation strategy is based on an MTPA approach, aimed to minimize the rms current for a given reference torque. The approach can be also applied to chosen subsets of the machine windings and is, therefore, suitable for independent torque control strategies.

The whole control algorithm has been experimentally validated in several testing scenarios, showing both the generality and the flexibility of the proposed approach.

Future works will show how the proposed approach can be also adapted to different kinds of machines, like synchronous reluctance machines, interior PMSMs and induction machines.

Appendix A

This section describes how the configuration matrix $\boldsymbol{U}_f$ can be computed from the constraints matrix $\boldsymbol{M}$ and justifies the properties summarized in (8).

Given the full-ranked $n \times n_c$ constraints matrix $\boldsymbol{M}$, its singular value decomposition is given by the matrix product

$$\boldsymbol{M} = \boldsymbol{U} \cdot \boldsymbol{\Sigma} \cdot \boldsymbol{V}^{\mathrm{T}} = \begin{bmatrix} \boldsymbol{U}_c \, \boldsymbol{U}_f \end{bmatrix} \cdot \begin{bmatrix} \tilde{\boldsymbol{\Sigma}} \\ \boldsymbol{0} \end{bmatrix} \cdot \boldsymbol{V}^{\mathrm{T}} = \boldsymbol{U}_c \cdot \tilde{\boldsymbol{\Sigma}} \cdot \boldsymbol{V}^{\mathrm{T}} \tag{26}$$

where $\boldsymbol{U}$ is a unitary $n \times n$ matrix, $\boldsymbol{V}$ is a unitary $n_c \times n_c$ matrix, and $\boldsymbol{\Sigma}$ is a $n \times n_c$ matrix. The $n_c \times n_c$ matrix $\tilde{\boldsymbol{\Sigma}}$ is a diagonal matrix whose diagonal elements (named singular values of $\boldsymbol{M}$) are all positive. In (26), the columns of $\boldsymbol{U}$ (named left singular vectors of $\boldsymbol{M}$) have been grouped in the $n \times n_c$ matrix $\boldsymbol{U}_c$ and in the $n \times (n - n_c)$ matrix $\boldsymbol{U}_f$.

Proof that $\boldsymbol{U}_f^{\mathrm{T}} \cdot \boldsymbol{M} = \boldsymbol{0}$.

Since $\boldsymbol{U}$ is unitary, $\boldsymbol{U}^{\mathrm{T}} \cdot \boldsymbol{U} = \boldsymbol{I}$. The matrix product is

$$\boldsymbol{U}^{\mathrm{T}} \cdot \boldsymbol{U} = \begin{bmatrix} \boldsymbol{U}_c^{\mathrm{T}} \\ \boldsymbol{U}_f^{\mathrm{T}} \end{bmatrix} \cdot \begin{bmatrix} \boldsymbol{U}_c \, \boldsymbol{U}_f \end{bmatrix} = \begin{bmatrix} \left(\boldsymbol{U}_c^{\mathrm{T}} \cdot \boldsymbol{U}_c\right) & \left(\boldsymbol{U}_c^{\mathrm{T}} \cdot \boldsymbol{U}_f\right) \\ \left(\boldsymbol{U}_f^{\mathrm{T}} \cdot \boldsymbol{U}_c\right) & \left(\boldsymbol{U}_f^{\mathrm{T}} \cdot \boldsymbol{U}_f\right) \end{bmatrix} \tag{27}$$

and, being equal to the identity matrix, it results that

$$\boldsymbol{U}_c^{\mathrm{T}} \cdot \boldsymbol{U}_c = \boldsymbol{I},\ \boldsymbol{U}_f^{\mathrm{T}} \cdot \boldsymbol{U}_f = \boldsymbol{I},\ \boldsymbol{U}_f^{\mathrm{T}} \cdot \boldsymbol{U}_c = \boldsymbol{0}. \tag{28}$$

By premultiplying (26) for $\boldsymbol{U}_f^{\mathrm{T}}$ and by using (28) one gets

$$\begin{aligned} \boldsymbol{U}_f^{\mathrm{T}} \cdot \boldsymbol{M} &= \boldsymbol{U}_f^{\mathrm{T}} \cdot \left(\boldsymbol{U}_c \cdot \tilde{\boldsymbol{\Sigma}} \cdot \boldsymbol{V}^{\mathrm{T}}\right) \\ &= \left(\boldsymbol{U}_f^{\mathrm{T}} \cdot \boldsymbol{U}_c\right) \cdot \left(\tilde{\boldsymbol{\Sigma}} \cdot \boldsymbol{V}^{\mathrm{T}}\right) = \boldsymbol{0} \end{aligned} \tag{29}$$

which is indeed the first property of (8)

Proof that $\left(\boldsymbol{I} - \boldsymbol{U}_f \cdot \boldsymbol{U}_f^{\mathrm{T}}\right) \cdot \boldsymbol{i}_m = \boldsymbol{0}$.

By using (26) for $\boldsymbol{M}$ in the expression (5), it results that

$$\begin{aligned} \boldsymbol{0} = \boldsymbol{M}^{\mathrm{T}} \cdot \boldsymbol{i}_m &= \left(\boldsymbol{V} \cdot \tilde{\boldsymbol{\Sigma}}^{\mathrm{T}} \cdot \boldsymbol{U}_c^{\mathrm{T}}\right) \cdot \boldsymbol{i}_m \\ &= \left(\boldsymbol{V} \cdot \tilde{\boldsymbol{\Sigma}}\right) \cdot \left(\boldsymbol{U}_c^{\mathrm{T}} \cdot \boldsymbol{i}_m\right). \end{aligned} \tag{30}$$

Since both $\tilde{\boldsymbol{\Sigma}}$ and $\boldsymbol{V}$ are $n_c \times n_c$ invertible matrices, (30) implies that $\boldsymbol{U}_c^{\mathrm{T}} \cdot \boldsymbol{i}_m = \boldsymbol{0}$. Given that $\boldsymbol{U}$ is unitary, it also results $\boldsymbol{U} \cdot \boldsymbol{U}^{\mathrm{T}} = \boldsymbol{I}$. Then, set $\boldsymbol{i}_m$ can be expressed as

$$\begin{aligned}
\boldsymbol{i}_m &= \boldsymbol{I} \cdot \boldsymbol{i}_m = \left(\boldsymbol{U} \cdot \boldsymbol{U}^{\mathrm{T}}\right) \cdot \boldsymbol{i}_m = \ \ldots \\
\cdots &= \left(\begin{bmatrix} \boldsymbol{U}_c & \boldsymbol{U}_f \end{bmatrix} \cdot \begin{bmatrix} \boldsymbol{U}_c^{\mathrm{T}} \\ \boldsymbol{U}_f^{\mathrm{T}} \end{bmatrix} \right) \cdot \boldsymbol{i}_m = \ \ldots \\
\cdots &= \boldsymbol{U}_c \cdot \boldsymbol{U}_c^{\mathrm{T}} \cdot \boldsymbol{i}_m + \boldsymbol{U}_f \cdot \boldsymbol{U}_f^{\mathrm{T}} \cdot \boldsymbol{i}_m = \ \ldots \\
\cdots &= \boldsymbol{U}_c \cdot \boldsymbol{0} + \boldsymbol{U}_f \cdot \boldsymbol{U}_f^{\mathrm{T}} \cdot \boldsymbol{i}_m = \left(\boldsymbol{U}_f \cdot \boldsymbol{U}_f^{\mathrm{T}}\right) \cdot \boldsymbol{i}_m
\end{aligned} \tag{31}$$

and, by moving everything to the first term, it results that $(\boldsymbol{I} - \boldsymbol{U}_f \cdot \boldsymbol{U}_f^{\mathrm{T}}) \cdot \boldsymbol{i}_m = \boldsymbol{0}$, which is the second property of (8).

Naturally, this last property is also verified by the reference currents $\boldsymbol{i}_m^*$ and by the derivatives of the reference currents $\boldsymbol{\delta i}_m^*$ once they satisfy the same constraints requirement, thus justifying the statements in (11).

Note that this property does not imply that the $n \times n$ matrix $\boldsymbol{U}_f \cdot \boldsymbol{U}_f^{\mathrm{T}}$ is equal to the identity matrix, but only that any feasible current set $\boldsymbol{i}_m$ belongs to its null space.

Appendix B

In what follows, it is analytically shown that the voltage $\boldsymbol{v}_{\mathrm{VSI,opt}}^*$ found as per (13) performs the desired decoupling of the dynamics of the currents, represented by the condition (14).

By substituting the controller (13) into the system (10), by recalling that $(\boldsymbol{U}_f^{\mathrm{T}} \cdot \boldsymbol{N}) \cdot (\boldsymbol{U}_f^{\mathrm{T}} \cdot \boldsymbol{N})^{\dagger} = \boldsymbol{I}$ and by cancelling out the compensation terms $(\boldsymbol{U}_f^{\mathrm{T}} \cdot \boldsymbol{R} \cdot \boldsymbol{i}_m)$ and $(\boldsymbol{U}_f^{\mathrm{T}} \cdot \boldsymbol{e}_{\mathrm{PM}})$, it results

$$\boldsymbol{U}_f^{\mathrm{T}} \cdot \boldsymbol{L} \cdot \left(\frac{\mathrm{d}\boldsymbol{i}_m}{\mathrm{d}t} - \boldsymbol{\delta i}_m^* \right) = \boldsymbol{0}. \tag{32}$$

Since $(\boldsymbol{U}_f^{\mathrm{T}} \cdot \boldsymbol{L})$ is not a square matrix, (32) does not directly imply that $\mathrm{d}\boldsymbol{i}_m/\mathrm{d}t = \boldsymbol{\delta i}_m^*$. However, from (8) and (11), $\boldsymbol{i}_m = (\boldsymbol{U}_f \cdot \boldsymbol{U}_f^{\mathrm{T}}) \cdot \boldsymbol{i}_m$ and $\boldsymbol{\delta i}_m^* = (\boldsymbol{U}_f \cdot \boldsymbol{U}_f^{\mathrm{T}}) \cdot \boldsymbol{\delta i}_m^*$ and with some algebraic manipulation it results that

$$\left(\boldsymbol{U}_f^{\mathrm{T}} \cdot \boldsymbol{L} \cdot \boldsymbol{U}_f\right) \cdot \left[\frac{\mathrm{d}\left(\boldsymbol{U}_f^{\mathrm{T}} \cdot \boldsymbol{i}_m\right)}{\mathrm{d}t} - \left(\boldsymbol{U}_f^{\mathrm{T}} \cdot \boldsymbol{\delta i}_m^*\right) \right] = \boldsymbol{0}. \tag{33}$$

The matrix $(\boldsymbol{U}_f^{\mathrm{T}} \cdot \boldsymbol{L} \cdot \boldsymbol{U}_f)$ is symmetric and positive definite, so (33) is satisfied only when the second term of the product is zero, meaning that

$$\frac{\mathrm{d}\left(\boldsymbol{U}_f^{\mathrm{T}} \cdot \boldsymbol{i}_m\right)}{\mathrm{d}t} = \left(\boldsymbol{U}_f^{\mathrm{T}} \cdot \boldsymbol{\delta i}_m^*\right) \ . \tag{34}$$

Finally, by premultiplying (34) by $\boldsymbol{U}_f$ and by considering once again (8) and (11), it results

$$\frac{\mathrm{d}\left(\boldsymbol{U}_f \cdot \boldsymbol{U}_f^{\mathrm{T}} \cdot \boldsymbol{i}_m\right)}{\mathrm{d}t} = \left(\boldsymbol{U}_f \cdot \boldsymbol{U}_f^{\mathrm{T}} \cdot \boldsymbol{\delta i}_m^*\right) \ \Rightarrow \ \frac{\mathrm{d}\boldsymbol{i}_m}{\mathrm{d}t} = \boldsymbol{\delta i}_m^* \tag{35}$$

which is indeed the decoupling requirement (14).

References

[1] E. Levi, "Multiphase electric machines for variable-speed applications," *IEEE Trans. Ind. Electron.*, vol. 55, no. 5, pp. 1893–1909, May 2008.

[2] F. Barrero and M. J. Duran, "Recent advances in the design, modeling, and control of multiphase machines—Part I," *IEEE Trans. Ind. Electron.*, vol. 63, no. 1, pp. 449–458, Jan. 2016.

[3] M. J. Duran and F. Barrero, "Recent advances in the design, modeling, and control of multiphase machines—Part iI," *IEEE Trans. Ind. Electron.*, vol. 63, no. 1, pp. 459–468, Jan. 2016.

[4] Z. Liu, Y. Li, and Z. Zheng, "A review of drive techniques for multiphase machines," *CES Trans. Electr. Mach. Syst.*, vol. 2, no. 2, pp. 243–251, Jun. 2018.

[5] I. Zoric, M. Jones, and E. Levi, "Vector space decomposition algorithm for asymmetrical multiphase machines," in *Proc. Int. Symp. Power Electron.*, Oct. 2017, pp. 1–6.

[6] A. Cervone, M. Slunjski, E. Levi, and G. Brando, "Optimal third-harmonic current injection for asymmetrical multiphase permanent magnet synchronous machines," *IEEE Trans. Ind. Electron.*, vol. 68, no. 4, pp. 2772–2783, Apr. 2021.

[7] E. Jung, H. Yoo, S. Sul, H. Choi, and Y. Choi, "A nine-phase permanent-magnet motor drive system for an ultrahigh-speed elevator," *IEEE Trans. Ind. Appl.*, vol. 48, no. 3, pp. 987–995, May 2012.

[8] Y. Hu, Z. Q. Zhu, and M. Odavic, "Comparison of two-individual current control and vector space decomposition control for dual three-phase PMSM," *IEEE Trans. Ind. Appl.*, vol. 53, no. 5, pp. 4483–4492, Sep. 2017.

[9] J. Karttunen, S. Kallio, P. Peltoniemi, P. Silventoinen, and O. Pyrhönen, "Decoupled vector control scheme for dual three-phase permanent magnet synchronous machines," *IEEE Trans. Ind. Electron.*, vol. 61, no. 5, pp. 2185–2196, May 2014.

[10] S. Rubino, O. Dordevic, R. Bojoi, and E. Levi, "Modular Vector Control of Multi-Three-Phase Permanent Magnet Synchronous Motors," *IEEE Trans. Ind. Electron.*, doi: 10.1109/TIE.2020.3026271.

[11] S. Rubino, O. Dordevic, E. Armando, R. Bojoi, and E. Levi, "A Novel Matrix Transformation for Decoupled Control of Modular Multiphase PMSM Drives," *IEEE Trans. Power Electron.*, vol. 36, no. 7, pp. 8088–8101, Jul. 2021, doi: 10.1109/TPEL.2020.3043083.

[12] F. Locment, E. Semail, and X. Kestelyn, "Vectorial approach-based control of a seven-phase axial flux machine designed for fault operation," *IEEE Trans. Ind. Electron.*, vol. 55, no. 10, pp. 3682–3691, Oct. 2008.

[13] F. Baudart, B. Dehez, E. Matagne, D. Telteu-Nedelcu, P. Alexandre, and F. Labrique, "Torque control strategy of polyphase permanent-magnet synchronous machines with minimal controller reconfiguration under open-circuit fault of one phase," *IEEE Trans. Ind. Electron.*, vol. 59, no. 6, pp. 2632–2644, Jun. 2012.

[14] F. Yu, M. Cheng, and K. T. Chau, "Controllability and performance of a nine-phase FSPM motor under severe five open-phase fault conditions," *IEEE Trans. Energy Convers.*, vol. 31, no. 1, pp. 323–332, Mar. 2016.

[15] N. Bianchi, S. Bolognani, and M. D. Pre, "Strategies for the fault-tolerant current control of a five-phase permanent-magnet motor," *IEEE Trans. Ind. Appl.*, vol. 43, no. 4, pp. 960–970, Jul. 2007.

[16] S. Dwari and L. Parsa, "An optimal control technique for multiphase PM machines under open-circuit faults," *IEEE Trans. Ind. Electron.*, vol. 55, no. 5, pp. 1988–1995, May 2008.

[17] X. Kestelyn and E. Semail, "A vectorial approach for generation of optimal current references for multiphase permanent-magnet synchronous machines in real time," *IEEE Trans. Ind. Electron.*, vol. 58, no. 11, pp. 5057–5065, Nov. 2011.

[18] A. Mohammadpour and L. Parsa, "A unified fault-tolerant current control approach for five-phase PM motors with trapezoidal back EMF under different stator winding connections," *IEEE Trans. Power Electron.*, vol. 28, no. 7, pp. 3517–3527, Jul. 2013.

[19] A. Mohammadpour, S. Sadeghi, and L. Parsa, "A generalized fault-tolerant control strategy for five-phase PM motor drives considering star, pentagon, and pentacle connections of stator windings," *IEEE Trans. Ind. Electron.*, vol. 61, no. 1, pp. 63–75, Jan. 2014.

[20] A. Mohammadpour and L. Parsa, "Global fault-tolerant control technique for multiphase permanent-magnet machines," *IEEE Trans. Ind. Appl.*, vol. 51, no. 1, pp. 178–186, Jan. 2015.

[21] A. G. Yepes, F. D. Freijedo, J. Doval-Gandoy, Ó. López, J. Malvar, and P. Fernandez-Comesaña, "Effects of discretization methods on the performance of resonant controllers," *IEEE Trans. Power Electron.*, vol. 25, no. 7, pp. 1692–1712, Jul. 2010.

[22] A. G. Yepes, J. Malvar, A. Vidal, O. López, and J. Doval-Gandoy, "Current harmonics compensation based on multiresonant control in synchronous frames for symmetrical n-Phase machines," *IEEE Trans. Ind. Electron.*, vol. 62, no. 5, pp. 2708–2720, May 2015.

[23] A. G. Yepes, J. Doval-Gandoy, F. Baneira, D. Pérez-Estévez, and O. López, "Current harmonic compensation for n -Phase machines with asymmetrical winding arrangement and different neutral configurations," *IEEE Trans. Ind. Appl.*, vol. 53, no. 6, pp. 5426–5439, Nov. 2017.

Andrea Cervone (Student Member, IEEE) received the B.Sc. and M.Sc. degrees in electrical engineering in 2014 and 2017, respectively, from the University of Naples Federico II, Naples, Italy, where he is currently working toward the Ph.D. degree in electrical engineering.

His research interests include multilevel converters and electrical drives.

Obrad Dordevic (Member, IEEE) received the Dipl. Ing. degree in electronic engineering from the University of Belgrade, Belgrade, Serbia, in 2008, and the Ph.D. degree from the Liverpool John Moores University, Liverpool, U.K., in April 2013.

In December 2009, he was with the Liverpool John Moores University, as a Ph.D. Student, where he was appointed as a Lecturer in May 2013 and promoted to a Reader in power electronics in 2018. His main research interests include the areas of power electronics, electrostatic precipitators, and advanced variable speed multiphase drive systems.

Gianluca Brando received the M.S. (*cum laude*) and Ph.D. degrees in electrical engineering from the University of Naples Federico II, Naples, Italy, in 2000 and 2004, respectively.

From 2000 to 2012, he was a Postdoctoral Research Fellow with the Department of Electrical Engineering, University of Naples Federico II. Since 2012, he has been an Assistant Professor of Electrical Machines and Drives with the Department of Electrical Engineering and Information Technology, University of Naples Federico II. He has authored several scientific papers published in international journals and conference proceedings. His research interests include control strategies for power converters and electrical drives.